ACS APPLIED MATERIALS & INTERFACES

Research Article

www.acsami.org

Sodium/Lithium Storage Behavior of Antimony Hollow Nanospheres for Rechargeable Batteries

Hongshuai Hou, Mingjun Jing, Yingchang Yang, Yirong Zhu, Laibing Fang, Weixin Song, Chengchi Pan, Xuming Yang, and Xiaobo Ji*

College of Chemistry and Chemical Engineering, Central South University, Changsha, Hunan 410083, China

ABSTRACT: Sodium-ion batteries (SIBs) have come up as an alternative to lithium-ion batteries (LIBs) for large-scale applications because of abundant Na storage in the earth's crust. Antimony (Sb) hollow nanospheres (HNSs) obtained by galvanic replacement were first applied as anode materials for sodium-ion batteries and exhibited superior electrochemical performances with high reversible capacity of 622.2 mAh g^{-1} at a current density of 50 mA g^{-1} after 50 cycles, close to the theoretical capacity (660 mAh g^{-1}); even at high current density of 1600 mA g^{-1}, the reversible capacities can also reach 315 mAh g^{-1}. The benefits of this unique structure can also be extended to LIBs, resulting in reversible capacity of 627.3 mAh g^{-1} at a current density of 100 mAh g^{-1} after 50 cycles, and at high current density of 1600 mA g^{-1}, the reversible capacity is 435.6 $mAhg^{-1}$. Thus, these benefits from the Sb HNSs are able to provide a robust architecture for SIBs and LIBs anodes.

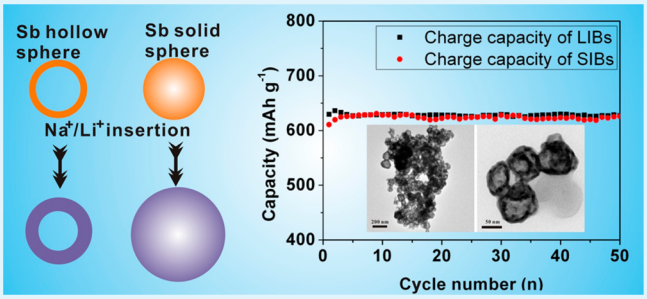

KEYWORDS: *antimony hollow nanospheres, galvanic replacement, sodium-ion battery, lithium-ion battery, anode*

1. INTRODUCTION

Large-scale storage requires a low cost, safe, and green battery system. Though lithium-ion batteries (LIBs) have been largely successful in the consumer electronics age, now it is becoming questionable, from not only the low abundance of lithium in the earth's crust (0.0065%) with the corresponding high cost but also a low efficient recycling. The rapidly increased demand of large-scale energy-storing devices, such as electric vehicle and stationary storage for renewable energies, accelerates the development of cheaper rechargeable batteries. Since that sodium is an earth abundant material (2.8% in the earth's crust) and sodium-ion batteries (SIBs) can meet these requirements better than LIBs, SIBs have come up as a more suitable alternative to LIBs for these applications.[1−4]

One of the main obstacles to the commercialization of SIBs is the limited choice of anode materials that can provide good stability and a high-rate performance. Now developing novel efficient Na storage anode materials becomes extremely urgent. Antimony (Sb) has long been considered as a promising anode material for high-energy density LIBs owing to its high theoretical capacity of 660 $mAhg^{-1}$ upon full lithiation to Li_3Sb.[5] Actually, one Sb atom can also maximally react with three Na atoms to form the Na_3Sb alloy,[6] reaching a theoretical capacity of 660 mAh g^{-1}. However, the large amount of sodium insertion/extraction into/from Sb causes a large volume change (up to approximately 390%),[7] which causes pulverization of Sb anode and loss of contact with the current collector, resulting in poor electrochemical performance.[8] Thus far, several kinds of Sb-based materials as anode for SIBs have been reported and demonstrated efficient Na storage in Sb-based materials, including Sb/C fibers,[6,9] mechanically milled Sb/C nanocomposites,[10] Sb/carbon nanotube nanocomposites,[8] monodisperse Sb nanocrystals,[5] reduced graphene oxide/nano Sb composite,[11] Mo_3Sb_7 alloy,[12] Zn_4Sb alloy,[13] SnSb alloy,[14] three-dimensional porous Sb/Cu_2Sb,[7] antimony sulfide nanoparticle-decorated graphene composite,[15] etc. Though some of them actually showed good electrochemical performance, most of the above-mentioned materials suffered from several drawbacks, such as low reversible capacity, poor capacity retention, high cost, poor scalability, and compatibility. Hence, more efficient, simple, and low cost methods to prepare high-performance Sb-based anodes should also be developed.

Hollow nanostructured materials have been explored for energy storage applications because of its special structure (high surface area, low density, high loading capacity, and shell permeability) which exhibits excellent properties such as excellent cycle stability and outstanding electronic transport properties.[16] Kim and Cho[17] synthesized Sb hollow nanoparticles from CTAB-functionalized SiO_2 templates. When used as anode for LIBs, the hollow nanoparticles electrode exhibited high capacity retention and excellent rate performance. However, this type conventional template method was too complicated and time-consuming. First, the templates should be modified to give them the ability to coax precursors onto the surface of the template core. Then, after the shell is decorated outside the scaffold, the templates must be eliminated in some

Received: July 2, 2014
Accepted: August 20, 2014
Published: August 20, 2014

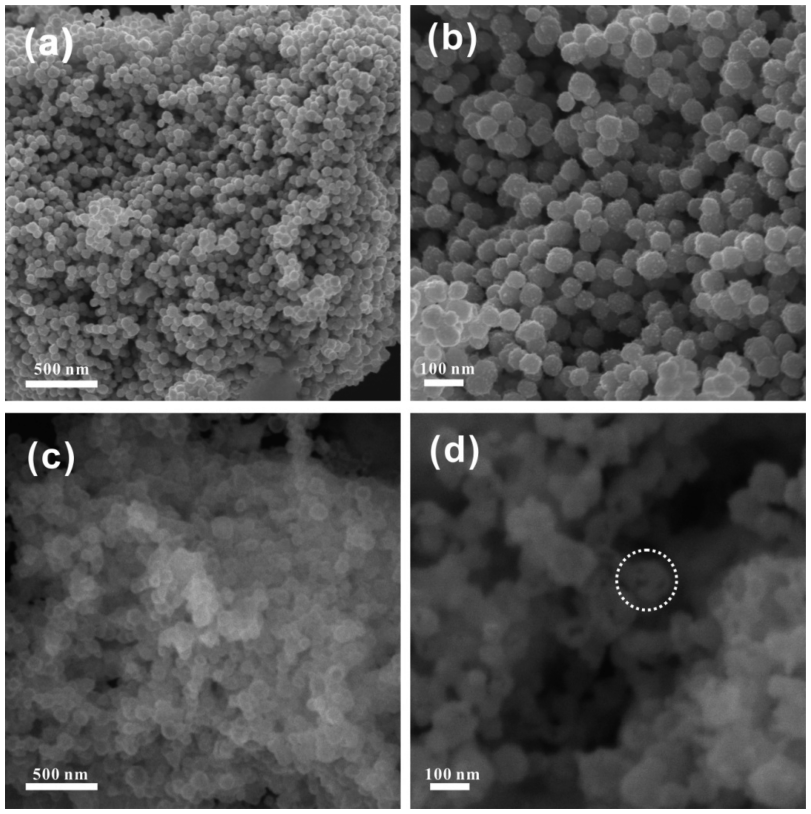

Figure 1. SEM images of Ni NSs (a, b) and Sb HNSs (c, d).

way, leaving behind a hollow shell. The shell growth and template removal are extremely complicated and energy-consuming, bringing additional problems on the product quality and process cost. In comparison, galvanic replacement is a simple, low cost, and green method to prepare some hollow metal nanostructures, such as nanoboxes, nanospheres, and nanotubes.[18]

Notably, Sb has not been reported in the form of hollow nanospheres as anode materials for SIBs. In this paper, we first reported the facile preparation of Sb hollow nanospheres (HNSs) by galvanic replacement; the unique structure led to the enhanced surface-to-volume ratio, alleviated volume change, and reduced transport lengths for both mass and charge transport. Herein, the Sb HNSs electrode exhibited excellent cycle stability and rate performance for SIBs, and the benefits of this unique structrue can also be extended to LIBs. It is believed that this green, facile, and convenient methodology will broaden new routes toward synthesizing other advanced energy-storing materials.

2. EXPERIMENTAL SECTION

2.1. Preparation of Ni NSs. 1.4 g of $NiCl_2 \cdot 6H_2O$ was dissolved in 60 mL of ethanol, and the desired pH of the solution was adjusted from 10 to 12 using 1 mol/L sodium hydroxide solution with vigorous stirring at 70 °C; then, 10 mL of hydrazine monohydrate (80 wt %) was added. After 30 min, the product was collected by centrifugation and washed several times with deionized water and ethanol.

2.2. Preparation of Sb HNSs. 0.1 g of the as-prepared Ni NSs was added to 50 mL of glycerol, and the suspension was sonicated for 30 min to ensure that the nanospheres were fully dispersed. Then, the $SbCl_3$ solution (0.6 g of $SbCl_3$ in 50 mL of glycerol) was subsequently added with magnetic stirring at 100 °C; vigorous stirring at 100 °C was maintained throughout all syntheses under an N_2 atmosphere. After 10 h, all the resultant products were centrifuged and washed with deionized water, followed by washing with ethanol.

2.3. Materials Characterization. Scanning electron microscopy (SEM, FEI Quanta 200), transmission electron microscopy (TEM, JEM-2100F), and X-ray diffraction (XRD, Rigaku D/max 2550 VB+ 18 kW, Cu Kα radiation) were used to characterize the morphology and composition of the hollow nanospheres.

2.4. Electrochemical Characterization. For electrochemical performance evaluation, CR2016 coin cells were assembled in an argon filled glovebox. The as-prepared Sb HNSs powder was mixed with super P and a carboxymethyl cellulose (CMC) binder (70:15:15 in weight) in deionized water to form a homogeneous slurry, which was painted on a copper foil. After solvent evaporation, the electrode was pressed and dried at 100 °C under vacuum for 12 h. Na metal foil was used as the counter electrode, and Celgard 2400 was used as the separator. The electrolyte was a solution of 1 M $NaClO_4$ in propylene carbonate electrolyte with 5% fluoroethylene carbonate (FEC) additive. For the lithium storage performance test, Li metal foil was used as the counter electrode, and Celgard 2400 was used as the separator. The electrolyte was a solution of 1 M $LiPF_6$ in ethylene carbonate/dimethyl carbonate (1:1 in volume) electrolyte with 5% fluoroethylene carbonate (FEC) additive. Cyclic voltammetric measurements were performed on Solartron Analytical to examine the cathode and anode reaction using the above-mentioned cell in the voltage range of 2−0.01 V (vs Na/Na^+ or Li/Li^+) at a scan rate of 0.1 mV s^{-1}. Galvanostatic charge−discharge tests were performed on the LAND battery system (CT2001A) at a suitable current density between 0.01 and 2 V (vs Na/Na^+ or Li/Li^+) for both charge (Na^+ or Li^+ extraction) and discharge (Na^+ or Li^+ insertion) at room temperature. The electrochemical impedance measurements were performed on Solartron Analytical at an AC voltage of 5 mV amplitude in the 100 kHz to 0.01 Hz during the 25th discharge−charge cycle for both SIBs and LIBs.

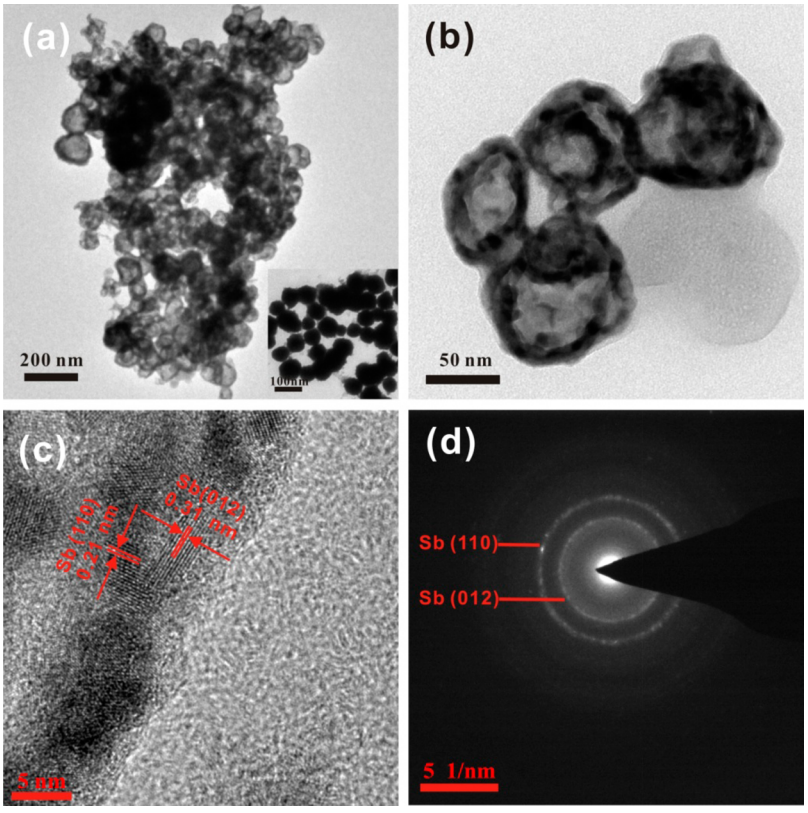

Figure 2. TEM image of Ni NSs (inset of a). TEM (a, b) and HRTEM (c) images and SAED pattern (d) of Sb HNSs.

3. RESULTS AND DISCUSSION

Figure 1a,b displayed the scanning electron microscope (SEM) images of Ni NSs templates, showing that the as-prepared Ni templates were regular spheres with rough surfaces and the diameters were in the range of 50−80 nm. Figure 1c,d showed the SEM images of the obtained Sb HNSs. From low-magnification SEM image (Figure 1c), the Sb HNSs displayed spherical morphology with a uniform size distribution ranging from 70 to 100 nm. The interior structures of the prepared Sb HNSs can be further revealed by the SEM images of broken spheres. Figure 1d gave magnified SEM images of the spherical Sb samples collapsed or broken, clearly showing the hollow characteristic structure for the synthesized spherical Sb samples. Additionally, the agglomeration of Sb HNSs was observed in the high-magnification SEM image (Figure 1d).

Figure 2a represented the low-magnification transmission electron microscope (TEM) image of Sb HNSs; the obvious contrast between the dark edge and the pale central part confirmed that the interior of the as-prepared nanospheres was hollow, consistent with SEM observations. The inset of Figure 2a was the TEM image of original Ni templates with spherical morphology and solid interior in accord with the SEM results. Figure 2b displayed a high-magnification TEM image of Sb HNSs with an average diameter of about 10 nm. The high resolution TEM (HRTEM) image (Figure 2c) and selected area electron diffraction (SAED) (Figure 2d) clearly showed the polycrystalline texture of the Sb HNSs, and the corresponding HRTEM image of the HNSs exhibited good crystalline and clear lattice fringes. The interlayer distance was found to be 0.21 and 0.31 nm, which correspond to the (1 1 0) and (0 1 2) plane of Sb, respectively. Two ring patterns were observed in the SAED (Figure 2d) pattern of Sb HNSs, the inner ring corresponds to (1 1 0) plane and outer ring corresponds to (0 1 2) plane of Sb, respectively.

The X-ray diffraction (XRD) patterns of the as-synthesized Ni NSs and Sb HNSs were depicted in Figure 3. All the

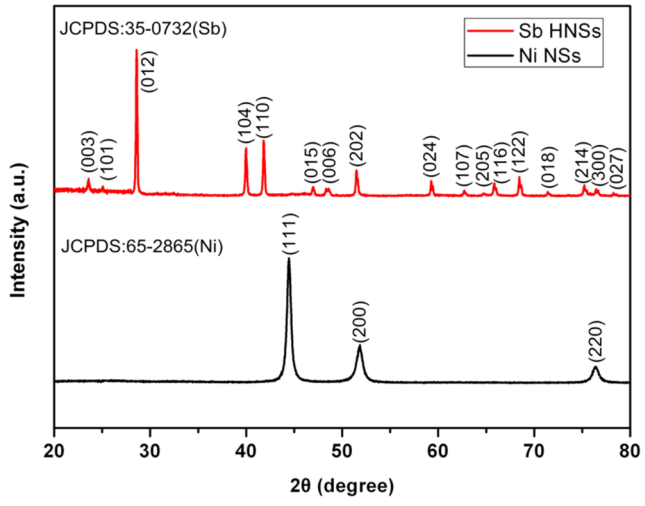

Figure 3. XRD patterns of Ni NSs and Sb HNSs.

diffraction peaks can be indexed to the standard diffraction data of the corresponding Ni (JCPDS: 65-2865) and Sb (JCPDS: 35-0732). The original Ni NS template was identified on the basis of the clearly distinguishable diffraction peaks at 44.493°, 51.846°, and 76.376°, corresponding to (1 1 1), (2 0 0), and (2 2 0) crystal planes of Ni. The peaks around 23.688°, 25.150°, 28.690°, 40.077°, 41.947°, 47.071°, 48.430°, 51.894°, 59.387°, 62.773°, 64.828°, 65.910°, 68.537°, 71.526°, 75.302°, 76.588°,

dx.doi.org/10.1021/am504310k | ACS Appl. Mater. Interfaces 2014, 6, 16189−16196

and 78.380° were observed, corresponding to (0 0 3), (1 0 1), (0 1 2), (1 0 4), (1 1 0), (0 1 5), (0 0 6), (2 0 2), (0 2 4), (1 0 7), (2 0 5), (1 1 6), (1 2 2), (0 1 8), (2 1 4), (3 0 0), and (2 0 7) crystal planes of Sb; no secondary phases were observable. Hence, the obtained Sb HNSs were of high purity and in good crystallinity. The as-prepared Sb HNSs with polycrystalline texture were identified, which was in good agreement with HRTEM and SAED results (Figure 2c,d).

Scheme 1 illustrates the growth mechanism of the Sb HNSs. Since the Sb is more active than Ni, Ni nanosphere (NS) in

Scheme 1. Schematic of Sb HNS Formation during the Galvanic Replacement at Different Stages

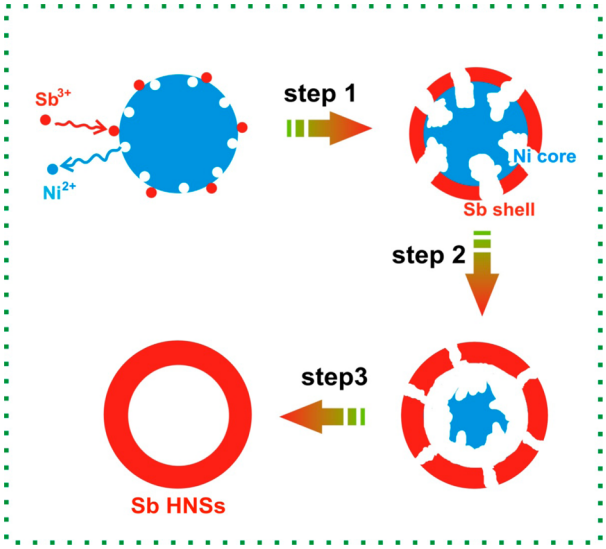

solution was attacked by Sb^{3+} and oxidized to Ni^{2+}, and Sb^{3+} was simultaneously reduced to Sb. The Sb atoms resulting from the galvanic replacement were deposited on the surface of Ni NS template. Since the replacement reaction was initiated locally rather than over the entire surface,[19] the deposition would lead to the formation of a porous Sb shell on each individual Ni NS template, and this shell could prevent the inside Ni surface from reacting with Sb^{3+}. As a result, only the holes in the newly formed Sb shells could serve as active sites for further reaction, allowing all the species involved in the reaction to continuously diffuse in and out of the holes until the Ni NS template was completely digested. Besides providing electrons, Ni NS template also served as support for Sb deposition and nucleation. Because of the existence of excessive Sb^{3+}, the replacement reaction was continuous, Sb continued nucleating on the Ni NS template surface, and Ni NS template continued to be consumed until it was completely consumed, which was confirmed by the TEM (Figure 2) and XRD (Figure 3) analysis. Finally, as observed in Figure 2a,b, all holes almost disappeared and each shell was characterized by a hole-free surface. The elimination of holes could be attributed to mass-transport processes such as Ostwald ripening.[20]

The electrochemical performance of the obtained Sb HNSs as anode for SIBs was studied. Figure 4a displayed the cyclic voltammograms (CVs) of Sb HNSs electrode for SIBs in the initial three cycles at a scan rate of 0.1 mV s^{-1} between 0.01 and 2 V (vs Na/Na^+). The cathodic peak at 0.27 V (peak 1) in the first cycle corresponds to the formation of a SEI layer and the conversion of crystalline Sb to the Na_xSb phase ($0 < x \leq 3$, eqs 1 and 2), respectively. The anodic peak at 0.85 V (peak 5) corresponds to the phase transition from the Na_xSb alloy to Sb ($0 < x \leq 3$, eqs 1 and 2). In the second and third cathodic process, three peaks at 0.31 (peak 2), 0.50 (peak 3), and 0.67 V (peak 4) were observed, and two peaks at 0.50 and 0.67 V can be ascribed to the generation of new Na_xSb phase phases.[8] The peak around 0.27 V (peak 1) during the first sodiation scan shifted to 0.31 V (peak 2) in the following sodiation. The difference between the first and subsequent cycles was probably due to the formation of the SEI layer. In addition, the CV curves of the following cycles were almost overlapped, indicating an excellent cycle stability of the Sb HNSs electrode.

$$Sb + xNa^+ + xe^- \leftrightarrow Na_xSb \quad (1)$$

$$Na_xSb + (3 - x)Na^+ + (3 - x)e^- \leftrightarrow Na_3Sb \quad (2)$$

Figure 4b showed the charge−discharge curves of the Sb HNSs electrode for 1st, 2nd, 3rd, 20th, and 50th cycle under a constant current density of 50 mA g^{-1}. As shown in Figure 5b, the voltage profiles showed sloping plateau lines during both charge and discharge, which were consistent with the peaks observed during CV scans. The sodiation capacity for the first cycle was 783.7 mAh g^{-1} with a Coulombic efficiency of around 77%. The low efficiency of the first cycle was mainly attributed to the irreversible formation of the SEI film on the surface of the Sb HNSs electrode during the first sodiation process. The sodiation capacities of the second and third cycle were 646.4 and 646.5 mAh g^{-1}, and corresponding Coulombic efficiencies were around 97% and 98%, respectively. For the reaction with Na, the first discharge (Na-ion insertion) was characterized by a wide flat plateau near 0.40 V whereas the second discharge has a notable sloping plateau between 0.5 and 0.75 V. During charges (Na-ion removal), the reaction was represented by a sloping plateau from 0.70 to 1.0 V. Remarkably, the correlative plateau regions can be observed in all 50 charge−discharge profiles of the Sb HNSs.

The cycle performance of Sb HNSs for SIBs is shown in Figure 4c. As can be seen, the Sb HNSs electrode showed superior cycle performance, delivering a high reversible capacity of 622.2 mAh g^{-1} after 50 cycles which is in close proximity to the theoretical capacity (660 mAh g^{-1}) of Sb. The Coulombic efficiency for the first cycle is around 77%, while it stabilized at ~98% for the following cycles.

The rate performance of the Sb HNSs for SIBs was investigated at various currents ranging from 50 to 1600 mA g^{-1}. As shown in Figure 4d, when increasing the current density, Sb HNSs exhibited good reversible capacity retention: 628 mAh g^{-1} (50 mA g^{-1}), 605 mAh g^{-1} (100 mA g^{-1}), 563 mAh g^{-1} (200 mA g^{-1}), 521 mAh g^{-1} (400 mA g^{-1}), 402 mAh g^{-1} (800 mA g^{-1}), and 315 mAh g^{-1} (1600 mA g^{-1}). When the current density went back to 50 mA g^{-1}, the reversible capacity returned to 603 mAh g^{-1}, which was comparable to the initial reversible capacity at 50 mA g^{-1}, indicating the electrode was stable and had high reversibility.

As anode for SIBs, Sb HNSs exhibited superior cycle stability and rate performance. The Li storage performance was also investigated. As shown in Figure 5a, the peak (peak 1) located at around 0.65 V was observed in the first lithiation process, which was ascribed to both the lithiation of Sb and the decomposition of the electrolyte to form solid electrolyte interphase (SEI) film, corresponding to capacity loss during the first cycle. From the second cycle onward, a distinct peak (peak 2) at 0.82 V was found, which may be attributed to the

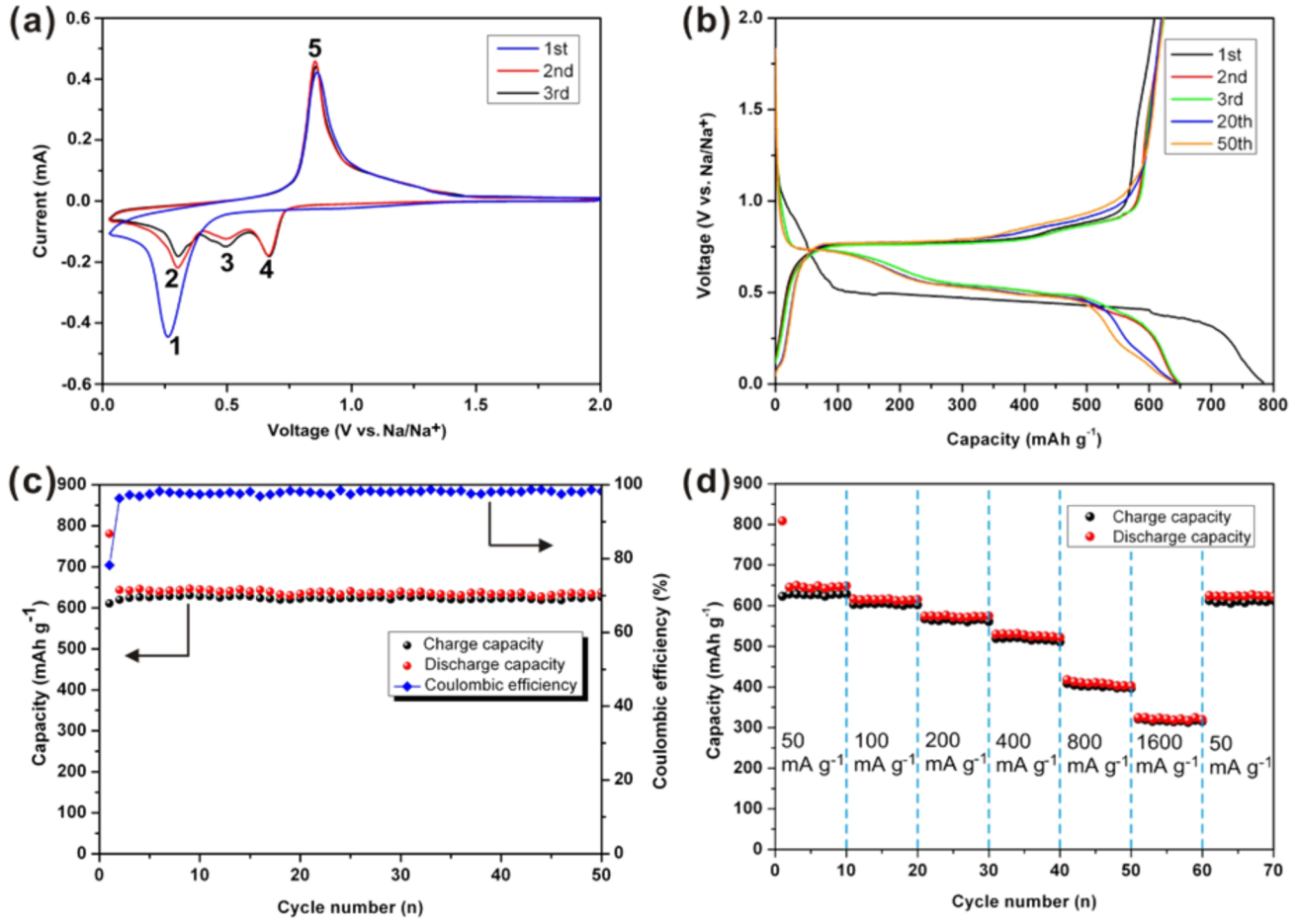

Figure 4. Cyclic voltammograms (a), galvanostatic charge−discharge profiles (b), cycle performance (c), and rate performance (d) of Sb HNSs anode for SIBs.

formation of Li_xSb alloy ($0 < x \leq 3$, eq 3). In the anodic sweep, the oxidation peak (peak 3) at 1.05 V was assigned to the dealloying reaction of Li_xSb ($0 < x \leq 3$, eq 3).[5] All peaks were reproducible and stabile after the first cycle, implying the reversibility of the electrochemical reactions of Sb HNSs electrode.

$$Sb + xLi^+ + xe^- \leftrightarrow Li_xSb \quad (3)$$

The voltage profiles of Sb HNSs for the 1st, 2nd, 3rd, 20th, and 50th cycle are shown in Figure 5b. For the reaction with Li, the first discharge (Li-ion insertion) was characterized by a wide flat plateau near 0.80 V whereas the following discharge has one flat plateau around 0.82 V. During both charges (Li-ion removal), the reaction was represented by one plateau around 1.05 V. The discharge plateaus at 0.82 V and charge plateau at ~1.05 V were related to the reversible Li−Sb alloying/dealloying reactions, consistent with CVs. The first cycle discharge and charge capacities were 798.2 and 629.6 mAh g^{-1}, which was close to the theoretical capacity (660 mAh g^{-1}). The Coulombic efficiency for the first cycle was around 79%, while it stabilized at ~98% for the following cycles. The flat plateau regions for both charge and discharge processes were obvious and wide. In addition, the voltage profiles of the following cycles almost overlapped, indicating an excellent cyclability of the Sb HNSs electrode. The plateau regions can be observed in all 50 charge−discharge profiles of the Sb HNSs and almost overlapped, indicating superior cycle stability.

Figure 5c depicted the cycle performance and Coulombic efficiency of Sb HNSs for LIBs over the investigated 50 cycles at a current density of 100 mA g^{-1}. The reversible capacity of the Sb HNSs electrode remained very stable from 629.6 mAh g^{-1} at the first cycle to 627.3 mAh g^{-1} after 50 cycles, showing a high capacity retention of 99.6%.

The rate performance of HNSs was investigated for LIBs at different current densities, from 50 to 1600 mA g^{-1}. As presented in Figure 5d, the charge capacities at current densities of 50, 100, 200, 400, 800, and 1600 mAg^{-1} were 633.0, 625.7, 602.7, 560.8, 516.3, and 435.6 mAh g^{-1}, respectively. When the current density went back to 50 mA g^{-1}, the reversible capacity returned to 621.5 mAh g^{-1}, which was comparable to the initial reversible capacity at 50 mA g^{-1}, indicating the electrode was stable and had high reversibility. From the electrochemical test results (Figures 4c and 5c), it can be seen that the Sb HNSs electrode displayed excellent cycle stability. Nevertheless, in comparison, the rate performance of Sb HNSs for SIBs was poorer than that for LIBs (Figures 4d and 5d). This is mainly limited by the slow Na ion diffusion kinetics, resulting from the large size of the Na ion (372% larger in volume than the Li ion for a coordination number of four; R_{Li} = 59 pm, R_{Na} = 99 pm).[4]

Electrochemical impedance spectroscopy (EIS) measurements of Sb HNSs electrode for SIBs and LIBs were conducted to evaluate the resistance against charge and ion transfer during cycles. As shown in Figure 6, each plot consisted of a semicircle

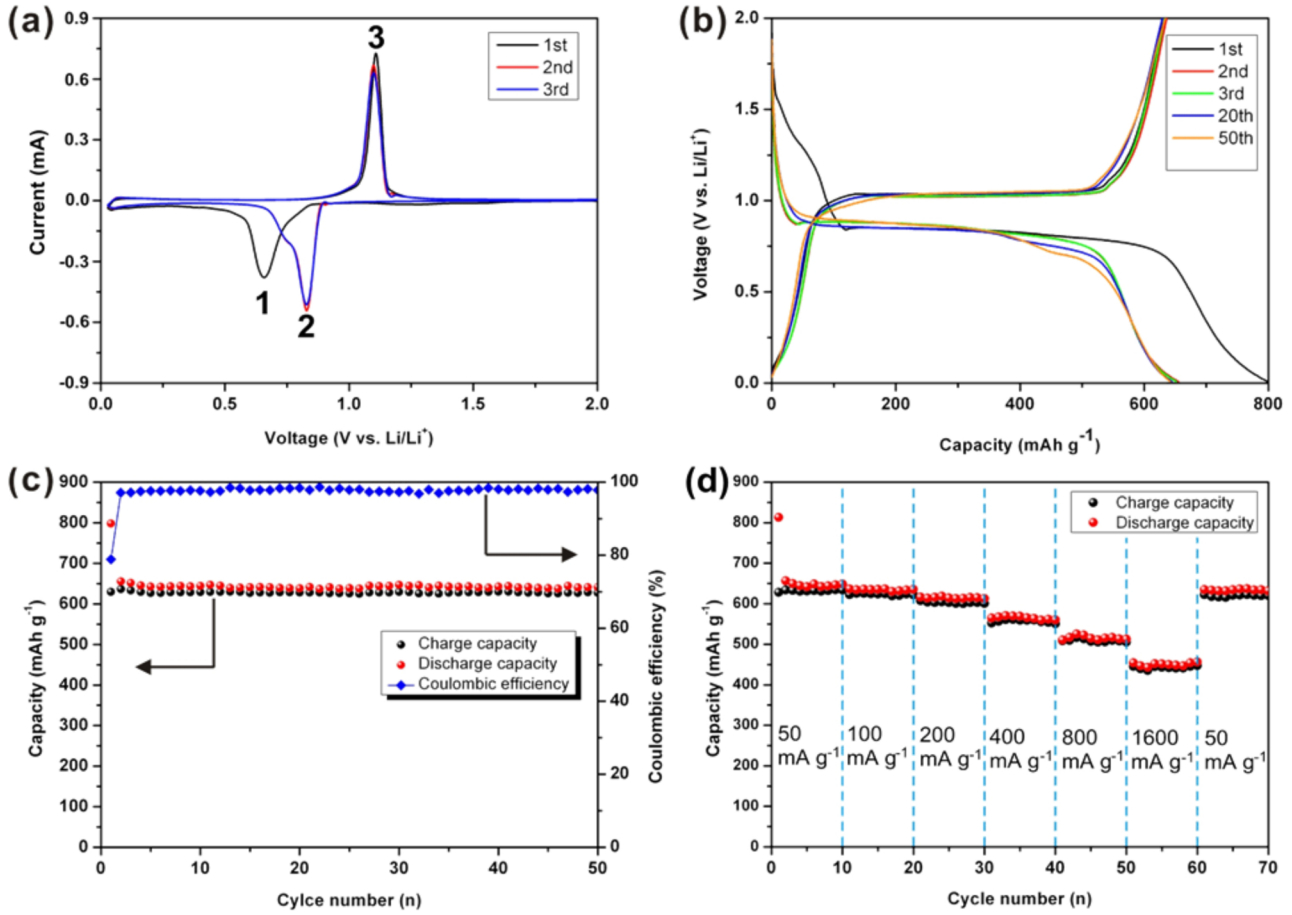

Figure 5. Cyclic voltammograms (a), galvanostatic charge−discharge profiles (b), cycle performance (c), and rate performance (d) of Sb HNSs anode for LIBs.

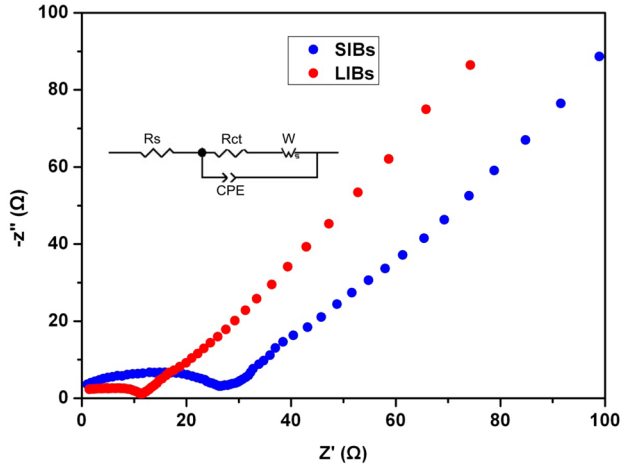

Figure 6. Nyquist plots and equivalent circuit (inset) of Sb HNSs electrode for SIBs and LIBs.

in the high frequency region attributed to the charge transfer process, and a slope in the low-frequency region of the impedance curve was related to the Na^+/Li^+ diffusivity of the active electrode material.[7] According to the radius of these semicircles in the high-frequency region, the charge-transfer impedance (Rct) of LIBs was lower than that of SIBs and, at lower frequency, LIBs were also shown to possess lower impedance (W), suggesting a sluggish kinetics of sodium uptake/release from Sb compared to a fast lithium uptake/release process, which further demonstrated the reason for poorer rate performance of SIBs compared with LIBs. The inset in Figure 6 showed the equivalent circuit model for the EIS studies. The Sb HNSs anode for SIBs displayed charge-transfer impedance (Rct) of 26.3 Ω, whereas the LIBs showed only 12.5 Ω, which was less than the SIBs.

The superior electrochemical performance of Sb hollow nanospheres is attributed to the specific characteristics of this unique hollow nanosphere structure. First, specific hollow interior of the Sb HNSs can effectively accommodate the dramatic volume change (Scheme 2) and alleviate the strain during Na^+/Li^+ insertion and extraction.[17,21,22] Second, the well-connected Sb hollow structure ensures an efficient and continuous electron transport. Third, high electrode/electrolyte contact area offers a large number of active sites for charge-transfer reaction, and the kinetics of the electrochemical reaction were enhanced. Last but not least, the very thin shell thickness (~10 nm) guarantees a very short Na^+/Li^+ diffusion distance (Scheme 3), which plays a vital role in the rate performance.[23]

Sb-based materials as anodes for SIBs have been studied by some researchers. However, Sb HNSs were first applied as anode for SIBs. Compared with previous Sb-based anodes,[5−15] Sb HNSs anodes prepared by galvanic replacement have lower cost and comparable electrochemical performance; they will be a promising candidate of anode materials for high performance SIBs.

Scheme 2. Schematic of the Volume Change during the Na^+/Li^+ Insertion of Sb HNSs and NSs

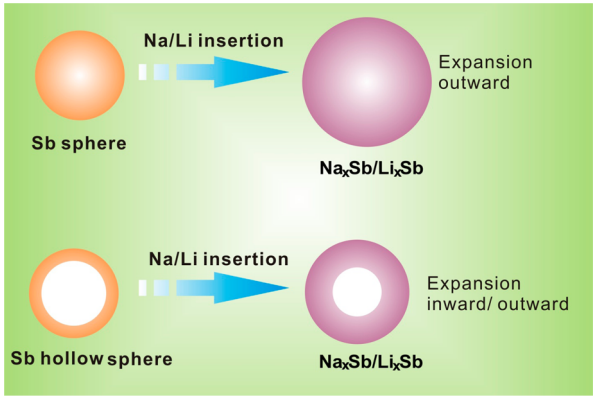

Scheme 3. Schematic of the Na^+/Li^+ Diffusion Process of Sb HNSs and NSs

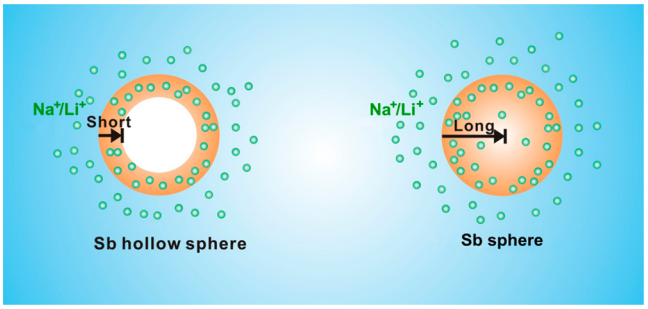

4. CONCLUSIONS

In summary, Sb HNSs prepared by galvanic replacement exhibited significantly improved cycle stability and rate performance for SIBs and LIBs. This improvement was largely attributed to the presence of hollow interiors that acted as buffer spaces for the volume change of the Sb thin shell which can also shorten the ion/charge diffusion length. In comparison with LIBs, SIBs presented lower rate capacities due to the slow Na ion diffusion kinetics, resulting from the large size of the Na ion. Sb HNSs were first used as anodes for SIBs, and they have a great potential as promising anode materials for high performance SIBs. This type of advanced hollow metallic nanosphere with special and unique characteristics provides an attractive application in electrochemical energy storage devices. It is believed that this green and convenient method will broaden new routes toward synthesizing other advanced energy-storing materials.

AUTHOR INFORMATION

Corresponding Author

*E-mail: xji@csu.edu.cn. Tel: +86 731-88879616. Fax: +86 731-88879616.

Notes

The authors declare no competing financial interest.

ACKNOWLEDGMENTS

This work was financially supported by the National Natural Science Foundation of China (21473258 and 21250110060), the Program for the New Century Excellent Talents in University (NCET-11-0513), and the Distinguished Young Scientists of Hunan Province (13JJ1004).

REFERENCES

(1) Ong, S. P.; Chevrier, V. L.; Hautier, G.; Jain, A.; Moore, C.; Kim, S.; Ma, X.; Ceder, G. Voltage, Stability and Diffusion Barrier Differences Between Sodium-Ion and Lithium-Ion Intercalation Materials. *Energy Environ. Sci.* **2011**, *4*, 3680−3688.

(2) Slater, M. D.; Kim, D.; Lee, E.; Johnson, C. S. Sodium-Ion Batteries. *Adv. Funct. Mater.* **2013**, *23*, 947−958.

(3) Song, W.; Ji, X.; Pan, C.; Zhu, Y.; Chen, Q.; Banks, C. E. A $Na_3V_2(PO_4)_3$ Cathode Material for Use in Hybrid Lithium Ion Batteries. *Phys. Chem. Chem. Phys.* **2013**, *15*, 14357−14363.

(4) Zhu, H.; Jia, Z.; Chen, Y.; Weadock, N.; Wan, J.; Vaaland, O.; Han, X.; Li, T.; Hu, L. Tin Anode for Sodium-Ion Batteries Using Natural Wood Fiber as a Mechanical Buffer and Electrolyte Reservoir. *Nano Lett.* **2013**, *13*, 3093−3100.

(5) He, M.; Kravchyk, K.; Walter, M.; Kovalenko, M. V. Monodisperse Antimony Nanocrystals for High-Rate Li-Ion and Na-Ion Battery Anodes: Nano Versus Bulk. *Nano Lett.* **2014**, *14*, 1255−1262.

(6) Wu, L.; Hu, X. H.; Qian, J. F.; Pei, F.; Wu, F. Y.; Mao, R. J.; Ai, X. P.; Yang, H. X.; Cao, Y. L. Sb-C Nanofibers with Long Cycle Life as an Anode Material for High-Performance Sodium-Ion Batteries. *Energy Environ. Sci.* **2014**, *7*, 323−328.

(7) Nam, D.-H.; Hong, K.-S.; Lim, S.-J.; Kwon, H.-S. Electrochemical Synthesis of a Three-Dimensional Porous Sb/Cu_2Sb Anode for Na-Ion Batteries. *J. Power Sources* **2014**, *247*, 423−427.

(8) Zhou, X.; Dai, Z.; Bao, J.; Guo, Y.-G. Wet Milled Synthesis of an Sb/MWCNT Nanocomposite for Improved Sodium Storage. *J. Mater. Chem. A* **2013**, *1*, 13727−13731.

(9) Zhu, Y.; Han, X.; Xu, Y.; Liu, Y.; Zheng, S.; Xu, K.; Hu, L.; Wang, C. Electrospun Sb/C Fibers for a Stable and Fast Sodium-Ion Battery Anode. *ACS Nano* **2013**, *7*, 6378−6386.

(10) Qian, J. F.; Chen, Y.; Wu, L.; Cao, Y. L.; Ai, X. P.; Yang, H. X. High Capacity Na-Storage and Superior Cyclability of Nanocomposite Sb/C Anode for Na-Ion Batteries. *Chem. Commun.* **2012**, *48*, 7070−7072.

(11) Nithya, C.; Gopukumar, S. rGO/nano Sb composite: A High Performance Anode Material for Na^+ Ion Batteries and Evidence for the Formation of Nanoribbons from Nano rGO Sheet During Galvanostatic Cycling. *J. Mater. Chem. A* **2014**, *2*, 10516−10525.

(12) Baggetto, L.; Allcorn, E.; Unocic, R. R.; Manthiram, A.; Veith, G. M. Mo_3Sb_7 as a Very Fast Anode Material for Lithium-Ion and Sodium-Ion Batteries. *J. Mater. Chem. A* **2013**, *1*, 11163−11169.

(13) Xu, J.; Wu, H.; Wang, F.; Xia, Y.; Zheng, G. Zn_4Sb_3 Nanotubes as Lithium Ion Battery Anodes with High Capacity and Cycling Stability. *Adv. Energy Mater.* **2013**, *3*, 286−289.

(14) Darwiche, A.; Sougrati, M. T.; Fraisse, B.; Stievano, L.; Monconduit, L. Facile Synthesis and Long Cycle Life of SnSb as Negative Electrode Material for Na-ion Batteries. *Electrochem. Commun.* **2013**, *32*, 18−21.

(15) Yu, D. Y.; Prikhodchenko, P. V.; Mason, C. W.; Batabyal, S. K.; Gun, J.; Sladkevich, S.; Medvedev, A. G.; Lev, O. High-Capacity Antimony Sulphide Nanoparticle-Decorated Graphene Composite as Anode for Sodium-Ion Batteries. *Nat. Commun.* **2013**, *4*, 2922−2926.

(16) Lai, X.; Halpert, J. E.; Wang, D. Recent Advances in Micro-/Nano-Structured Hollow Spheres for Energy Applications: From Simple to Complex Systems. *Energy Environ. Sci.* **2012**, *5*, 5604−5618.

(17) Kim, H.; Cho, J. Template Synthesis of Hollow Sb Nanoparticles as a High-Performance Lithium Battery Anode Material. *Chem. Mater.* **2008**, *20*, 1679−1681.

(18) Xia, X.; Wang, Y.; Ruditskiy, A.; Xia, Y. 25th Anniversary Article: Galvanic Replacement: A Simple and Versatile Route to Hollow Nanostructures with Tunable and Well-Controlled Properties. *Adv. Mater.* **2013**, *25*, 6313−6333.

(19) Sun, Y. G.; Xia, Y. N. Alloying and Dealloying Processes Involved in the Preparation of Metal Nanoshells through a Galvanic Replacement Reaction. *Nano Lett.* **2003**, *3*, 1569−1572.

(20) Sun, Y. G.; Mayers, B.; Xia, Y. N. Metal Nanostructures with Hollow Interiors. *Adv. Mater.* **2003**, *15*, 641−646.

(21) Yang, R.; Huang, J.; Zhao, W.; Lai, W.; Zhang, X.; Zheng, J.; Li, X. Bubble Assisted Synthesis of Sn−Sb−Cu Alloy Hollow Nanostructures and Their Improved Lithium Storage Properties. *J. Power Sources* **2010**, *195*, 6811−6816.
(22) Hou, H.; Tang, X.; Guo, M.; Shi, Y.; Dou, P.; Xu, X. Facile Preparation of Sn Hollow Nanospheres Anodes for Lithium-Ion Batteries by Galvanic Replacement. *Mater. Lett.* **2014**, *128*, 408−411.
(23) Tang, K.; Fu, L.; White, R. J.; Yu, L.; Titirici, M.-M.; Antonietti, M.; Maier, J. Hollow Carbon Nanospheres with Superior Rate Capability for Sodium-Based Batteries. *Adv. Energy Mater.* **2012**, *2*, 873−877.